High-temperature observation of intralayer, interlayer, and Rydberg excitons in bulk van der Waals alloy single crystals

Pravrati Taank,[1] Asif Ali,[1] Aravind Raji [●],[1] Ajay K. Poonia,[1]
Matthew C. Beard [●],[2] Ravi Shankar Singh [●],[1,*] and K. V. Adarsh [●][1,†]

[1]*Department of Physics, Indian Institute of Science Education and Research Bhopal, Bhopal 462066, India*
[2]*Chemistry & Nanoscience Center, National Renewable Energy Laboratory, Golden, Colorado 80401, USA*

Transition metal dichalcogenides exhibit remarkable optical properties due to the diverse number of strongly bound excitons, which can be fine-tuned by alloying. Despite a flurry of research activity in characterizing these excitons, a comprehensive and profound understanding of their behavior with temperature is lacking. Here, we report the rich spectrum of excitonic features within bulk van der Waals alloy $Mo_{0.5}W_{0.5}S_2$ and $Mo_{0.5}W_{0.5}Se_2$ single crystals through temperature-dependent reflectance spectroscopy and first-principles calculations. We observed Rydberg excitons and interlayer excitons in both the single crystals. Notably, we provide the first experimental evidence of highly energetic A′ and B′ excitons in $Mo_{0.5}W_{0.5}S_2$ at room temperature. The strong carrier-phonon scattering significantly broadens the A′, B′, and interlayer excitons at room temperature in bulk $Mo_{0.5}W_{0.5}S_2$ single crystal compared to its selenide. Our findings, supported by density functional theory and Bethe-Salpeter equation calculations, signify the crucial role of carrier-phonon interactions. These results open pathways for next-generation optoelectronic devices and quantum technologies operating at high temperature.

I. INTRODUCTION

Transition metal dichalcogenides (TMDs) have emerged as a new class of semiconductors for a wide range of applications in electronics and optoelectronics because of their remarkable properties like sizable band gaps [1], substantial spin-valley coupling [2,3], spin-layer locking [4,5], reduced dielectric screening [1,6], and strong Coulomb interactions resulting in the high binding energy of excitons [2,6,7]. These characteristics contribute to TMDs' rich and diverse landscape of excitonic transitions, positioning them at the forefront of optical technology, particularly in the domains of spintronics [8] and valleytronics [9]. For example, large spin-orbit coupling (SOC) in TMDs splits the valance and conduction bands at the K valley. This splitting results in the formation of low-energy intralayer A and B excitons and their excitonic Rydberg series [2,10–13]. Another example is interlayer excitons (IXs) at the K valleys, where electrons and holes residing in separate layers bind to form excitons based on spin-valley and spin-layer selection rules [3–5,14]. Also, some of the TMDs, such as selenides [15–18] and tellurides [15,18], show highly energetic A′ and B′ excitons; however, these excitons are not observed in sulfides. For more details, see Table S1 in the Supplemental Material (SM) [19] and in Refs. [3,4,15–18,20–26]. Overall, all these diverse excitons present in TMDs offer a wide range of potential optoelectronic applications, including optical quantum sensing [27], Bose-Einstein condensation [5,28], optical switching [12], and quantum information technology [29,30].

TMDs present unique opportunities for alloying through isoelectronic substitution of transition metal (M) or chalcogen (X) atoms, resulting in minimal lattice strain and the formation of quasibinary alloys that preserve the MX_2 structure [31–34]. This structural stability allows diverse excitons within these quasibinary alloys, mirroring those found in their binary counterparts. In principle, they can provide more fundamental insights than binary TMDs. For example, the right choice of atoms in an alloy offers a platform to tune the SOC and carrier-phonon scattering to explore a broader spectrum of excitons. Likewise, how the diverse excitons behave at different temperatures in TMDs is still lacking, which is essential for potential device applications.

Here, we present a comprehensive understanding of diverse excitonic features observed in the optical reflectance spectra of bulk $Mo_{0.5}W_{0.5}S_2$ and $Mo_{0.5}W_{0.5}Se_2$ alloy single crystals using temperature-dependent reflectance spectroscopy and first-principles calculations. In our experiments, we observed the Rydberg excitons of A exciton ($1s$ ground state) up to $n = 4$ quantum number, i.e., $2s$, $3s$, and $4s$ in $Mo_{0.5}W_{0.5}S_2$ single crystal. Other noteworthy findings are the first experimental observation of A′ and B′ excitons in transition metal sulfides at room temperature and the observation of IX between A and B excitons in both single crystals. The strong carrier-phonon scattering significantly broadens these excitons at room temperature in bulk $Mo_{0.5}W_{0.5}S_2$ single crystal compared to its selenide. Furthermore, our theoretical calculations concur well with the experimental results.

II. RESULTS AND DISCUSSION

Bulk $Mo_{0.5}W_{0.5}S_2$ and $Mo_{0.5}W_{0.5}Se_2$ alloy single crystals used in this study were procured from HQ Graphene.

---

*Contact author: rssingh@iiserb.ac.in
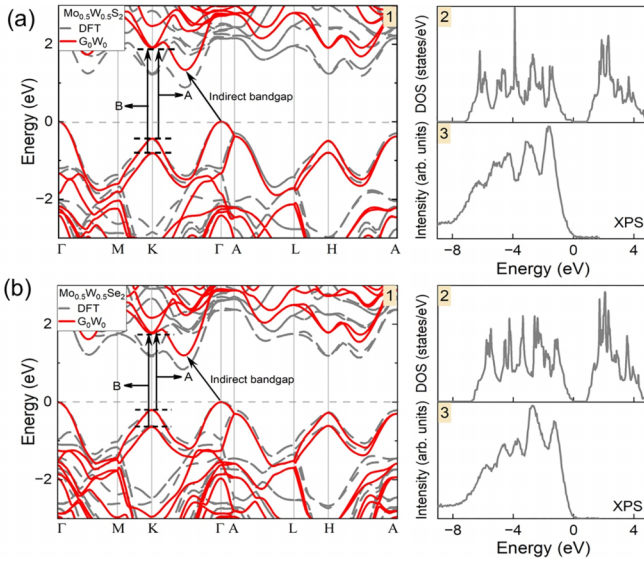†Contact author: adarsh@iiserb.ac.in

FIG. 1. Electronic band structure using DFT and G_0W_0 calculations of bulk (a) $Mo_{0.5}W_{0.5}S_2$ and (b) $Mo_{0.5}W_{0.5}Se_2$, (panel 1). The gray dashed line illustrates the Fermi levels. Panel 2 shows the calculated total DOS and panel 3 shows the room temperature experimental valence band spectra from x-ray photoemission spectroscopy for both single crystals.

These crystals underwent extensive characterization (x-ray diffraction, scanning electron microscopy, energy-dispersive x-ray spectra, and x-ray photoemission spectroscopy) to assess their structural and compositional properties. Details are provided in the SM [19]. Our measurements reveal the high quality and chemical purity of the single crystals.

A. Electronic structure of bulk $Mo_{0.5}W_{0.5}S_2$ and $Mo_{0.5}W_{0.5}Se_2$

Since the crystalline TMD of MX_2 displays large exciton binding energy and oscillator strength, we expect similar features in the optical and charge-transport properties of the alloy single crystals. For the identification of such diverse exciton species, we conducted a thorough investigation of the electronic structures of bulk $Mo_{0.5}W_{0.5}S_2$ and $Mo_{0.5}W_{0.5}Se_2$ within density functional theory (DFT) using the projector-augmented wave method [35] as implemented in the Vienna *Ab-Initio* Simulation Package (VASP) [36] with the exchange-correlation functional of Perdew-Burke-Ernzerhof [37]. Experimental lattice parameters were used for all calculations, and virtual crystal approximation (VCA) [38] was employed to represent the alloy compositions. The total density of state (DOS) calculations were done using the tetrahedron method. More details are in the SM [19] and in Refs. [39–42]. The calculated electronic band structures and DOS of $Mo_{0.5}W_{0.5}S_2$ and $Mo_{0.5}W_{0.5}Se_2$ are shown in Figs. 1(a) and 1(b) in panels 1 and 2. Our calculations reveal that both alloys exhibit an indirect band-gap nature, with the respective valence band maximum (VBM) situated at the Γ point and the conduction band minimum located between the K-Γ points in both DFT (gray) and G_0W_0 (red) calculations. Additionally, the introduction of SOC leads to a splitting of the VBM, resulting in the first direct band gap at the K point and the second direct band gap at the H point. Our

theoretical findings are consistent with the previously reported calculations in MoS_2 [43] and WS_2 [44] and highlight the significant contribution of transition metal d electrons to the band structure of these bulk alloy single crystals.

To understand the electronic structure of these systems, we compared the calculated DOS (panels 2) with the experimental valence band (panels 3) for bulk $Mo_{0.5}W_{0.5}S_2$ and $Mo_{0.5}W_{0.5}Se_2$ in Figs. 1(a) and 1(b), respectively. The observed valence band spectrum at room temperature exhibits semiconducting behavior with zero intensity at the Fermi level. The experimental valence band spectrum reveals five distinct features for $Mo_{0.5}W_{0.5}S_2$ and $Mo_{0.5}W_{0.5}Se_2$. These features reproduced in the calculated DOS are in good agreement with experimental valence band spectra. Furthermore, we compare the band dispersion with room-temperature angle-resolved photoemission spectroscopy (ARPES), revealing the SOC-driven K-valley splitting of ~0.37 eV in $Mo_{0.5}W_{0.5}Se_2$, as shown in Fig. S6 [19]. The DFT calculated band structure overlaid over the ARPES spectrum (Fig. S6 [19]) shows a good agreement suggesting that DFT with VCA is sufficient enough to capture the main features of the valence band in the case of bulk alloy single crystals.

B. Intralayer and Rydberg excitons at K valley

Bulk $Mo_{0.5}W_{0.5}S_2$ and $Mo_{0.5}W_{0.5}Se_2$ exhibit atomic stacking of the YY^* type, leading to 2H symmetry, as illustrated in Fig. S7 [19]. These bulk single crystals demonstrate a wide range of bright intralayer and interlayer excitons with notably high oscillator strengths. The former obeys the spin-valley selection rules, while the latter follows the spin-layer selection rules [4,45]. We conducted temperature-dependent reflectance spectroscopy to investigate these diverse optically active excitons and their impact on the optical properties of these single crystals. The detailed experimental procedure is in the SM [19]. Figures 2(a) and 2(b) display the reflectance spectra at a high temperature of 80 K for bulk $Mo_{0.5}W_{0.5}S_2$ and $Mo_{0.5}W_{0.5}Se_2$ single crystals, respectively. These spectra clearly demonstrate the presence of multiple optically active excitons.

To gain a deeper understanding, we conducted theoretical calculations of the absorption spectra by incorporating electron-hole interactions and solving the Bethe-Salpeter equation (BSE) with the Tamm-Dancoff approximation [46]. We considered the eight lowest conduction and eight highest valence bands for the BSE calculations. In Figs. 2(c) and 2(d), we present the theoretically calculated absorption spectra of bulk $Mo_{0.5}W_{0.5}S_2$ and $Mo_{0.5}W_{0.5}Se_2$, and the spectra are well in agreement with the experimental results in Figs. 2(a) and 2(b). These diverse spectral features observed in the experimental and theoretical spectra can be attributed to a range of excitonic transitions within the Brillouin zone, and their assignments are discussed in the following paragraphs.

First, we discuss the low-energy intralayer excitons, A and B, which are observed at ~1.915 and ~2.221 eV for $Mo_{0.5}W_{0.5}S_2$ and at ~1.603 and ~1.955 eV for $Mo_{0.5}W_{0.5}Se_2$. The A and B excitons originate from the splitting of the VBM due to strong SOC at the K point of the Brillouin zone [29,47]. The energy difference between the A and B excitons, which is an indicator of the strength of the SOC [21],
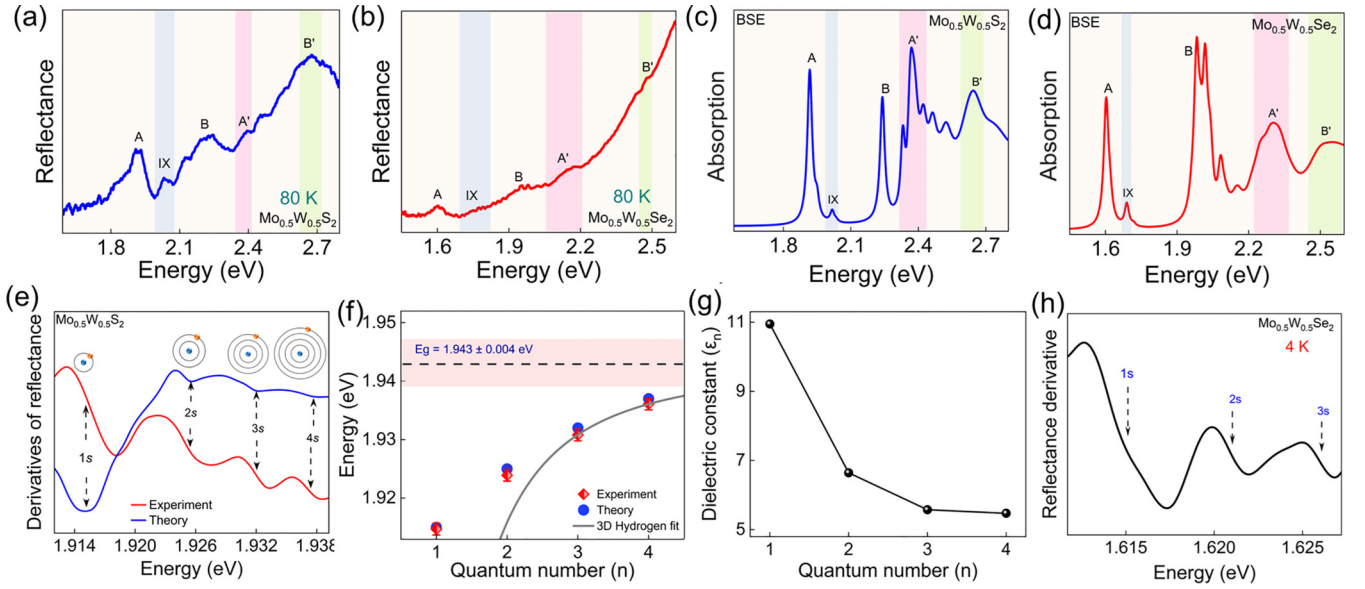
FIG. 2. Reflectance spectrum at 80 K for bulk (a) $Mo_{0.5}W_{0.5}S_2$ and (b) $Mo_{0.5}W_{0.5}Se_2$ single crystals. The blue, pink, and green regions show the interlayer (IX), A′, and B′ excitons, respectively. The theoretical absorption spectrum calculated using BSE for bulk (c) $Mo_{0.5}W_{0.5}S_2$ and (d) $Mo_{0.5}W_{0.5}Se_2$. (e) The first derivative of the experimentally measured reflectance spectrum and the second derivative of the theoretically calculated BSE absorption spectrum of bulk $Mo_{0.5}W_{0.5}S_2$ single crystal at 80 K. The peaks represent the Rydberg excitons up to $4s$ states, which follow Bohr's atomic model as shown schematically. Where blue and yellow balls are the nucleus (hole here) and the electron, respectively. The theoretical absorption spectra have been shifted by ~0.26 eV for better comparison with the experimental spectra. (f) Experimentally and theoretically obtained transition energies of the Rydberg series as a function of quantum number (n). The $n = 3$ and 4 peaks follow the 3D hydrogen model and the fit is represented by the gray line. The black dashed line and the pink shaded area show the estimated E_g and the uncertainty in the E_g value, respectively. (g) Calculated dielectric constants ϵ_n as a function of n. (h) The second derivative of the reflectance spectrum of bulk $Mo_{0.5}W_{0.5}Se_2$ single crystal at 4 K shows the Rydberg series up to $n = 3$.

is ~306 and ~352 meV in $Mo_{0.5}W_{0.5}S_2$ and $Mo_{0.5}W_{0.5}Se_2$, respectively. These values are in good agreement with our theoretical calculations, for the respective samples ~323 and ~378 meV. The fact that $Mo_{0.5}W_{0.5}Se_2$ exhibits a stronger SOC, as indicated by the larger energy difference between A and B excitons, compared to $Mo_{0.5}W_{0.5}S_2$ is due to the heavier chalcogen atom. This is further supported by the band structure calculations presented in Fig. 1. The A and B exciton positions in our BSE calculations are slightly overestimated compared to the experimental values due to overestimation of the band gap in G_0W_0 calculations.

To unravel the subtle characteristics of other excitonic transitions between A and B excitons, we have taken the first derivative of the reflectance spectrum of $Mo_{0.5}W_{0.5}S_2$ single crystal and plotted it in Fig. 2(e). On the higher-energy side of the A exciton known as the $1s$ ground state, we have obtained three additional peaks in Fig. 2(e). The intriguing aspect here lies in the gradual and continuous decrease in both peak intensities and energy separations as we move to higher energies being analogous to the excitonic Rydberg series [2]. So, we associate these fine structures as the excited states of A exciton up to $n = 4$ quantum number, i.e., $2s$, $3s$, and $4s$, since the energy separation and spectral weights resemble those of a hydrogen atom. Further, the transitions manifest as peaks situated between the $1s$ ground state and the quasiparticle band gap, as previously discussed in monolayer TMDs [2,11,48]. These s-like state transitions are dipole allowed and thus can be probed by linear optical spectroscopy [12]. Notably, our theoretical calculations also corroborate

this trend. The second derivative of the theoretically calculated absorption spectrum exhibits a similar pattern, with the minima in the curve pinpointing the energy positions of the Rydberg excitons. We observed similar features using the first derivative of the reflectance data (Fig. S9 [19]); however, the utilization of the second derivative enhances resolution, providing a more precise analysis. For clarity, we have outlined a schematic diagram in Fig. 2(e), aligning with Bohr's atomic model, where the electron resides in the corresponding shell. Furthermore, we have extracted the energy positions of these Rydberg excitons from the points of inflection of Fig. 2(e), and these positions are presented in Fig. 2(f) for a comprehensive view of the findings. Similar results are also obtained at 4 K (Fig. S10 [19]); however, Rydberg excitons disappear as the temperature increases beyond 80 K due to large carrier-phonon scattering [49]. Further, we observed the Rydberg series of excitons in $Mo_{0.5}W_{0.5}Se_2$ at 4 K [Fig. 2(h)].

From the exciton Rydberg series of the single crystal, we have computed the exciton binding energy using the formula typically used for three-dimensional (3D) Wannier excitons [50,51], given by $E_b^n = E_g - (R_y^*)/n^2$. Here, E_b^n, E_g, and R_y^* are the binding energy of the nth exciton, the quasiparticle band gap, and the effective Rydberg constant, respectively. We have used only $n = 3$ and 4 Rydberg excitons for fitting the data, since they are hydrogenic in nature, which is discussed later. The extracted value of $E_g = 1.943 \pm 0.004$ eV [black dashed line in Fig. 2(f)] and $E_b(= E_g - E_{A(1s)}) = 28 \pm 4$ meV. Notably, our observed binding energy values are
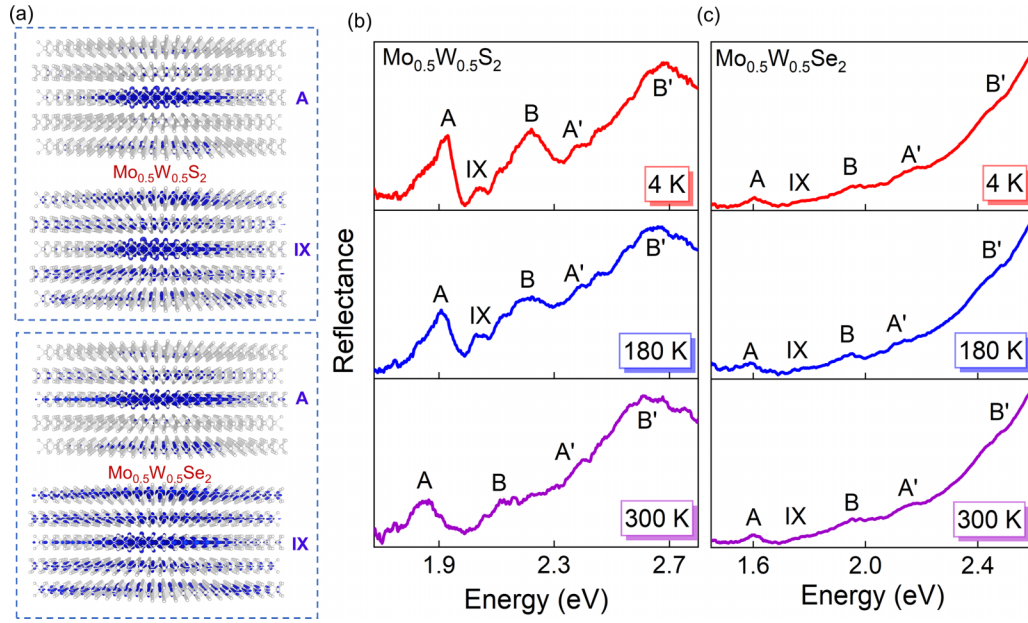
FIG. 3. (a) Spatial distribution of excitons shows the nature of A (intralayer) and IX excitons for $Mo_{0.5}W_{0.5}S_2$ (top panel) and $Mo_{0.5}W_{0.5}Se_2$ (bottom panel). Reflectance spectra as a function of temperature for bulk (b) $Mo_{0.5}W_{0.5}S_2$ and (c) $Mo_{0.5}W_{0.5}Se_2$ single crystals.

similar to those of GaSe [52], GaN [53], and ZnO [54] bulk single crystals, but at least an order of magnitude smaller than monolayer MoS_2 and WS_2 [2,10] due to the significantly large screening effect in the bulk material. To explain the observed nonhydrogenic behavior, we determined the nonuniform dielectric constant $\epsilon_n = \sqrt{\mu e^4 / (2\hbar^2 E_b^{(n)} n^2)}$ experienced by the Rydberg excitons [2], where μ represents the exciton reduced mass in terms of the electron rest mass (m_0) and is found to be $0.2471 m_0$, as estimated by DFT calculations at the K valley. Our results demonstrate a drastic reduction in ϵ_n for $n = 1$ and 2, while it remains nearly constant for $n = 3$ and 4 Rydberg excitons as shown in Fig. 2(g). This justifies the use of the 3D hydrogenic model for fitting $n = 3$ and 4, and the deviation from the hydrogenic model for $n = 1$ and 2 can be attributed to the antiscreening effect, consistent with previous reports in other TMDs [2,10] and semiconductors [55,56].

C. Direct interlayer excitons (IXs)

Another remarkable observation of our study is the identification of a distinctive spectral feature appearing at high energy to the A exciton by $\sim$114 meV in $Mo_{0.5}W_{0.5}S_2$ and $\sim$156 meV in $Mo_{0.5}W_{0.5}Se_2$, which is well below the B exciton within the reflectance spectrum [see Figs. 2(a) and 2(b)]. We assign these features to the direct IXs. Notably, our temperature-dependent studies presented in Fig. 3(b) show the weakening of the IX peak after 180 K in $Mo_{0.5}W_{0.5}S_2$; nevertheless, in $Mo_{0.5}W_{0.5}Se_2$, we could observe IX up to room temperature [Fig. 3(c)]. In contrast to the direct intralayer A exciton, these IXs exhibit reduced oscillator strength, strong dipole-dipole interactions, and lower binding energy. To provide a clearer understanding of the underlying mechanism, we have shown the schematic representation of band structure (Fig. S11 [19]) and spin configurations of IXs at the K valley in the YY^* stacked bulk alloy single crystal, considering two adjacent layers as depicted in Fig. S12 [19]. At each K point, the

band structure is composed of SOC split valence bands $V_1^{(\uparrow)}$ and $V_2^{(\downarrow)}$, as well as conduction bands $C_1^{(\uparrow)}$ and $C_2^{(\downarrow)}$ in layer 1 and with spin inversion in layer 2, referred to as spin-layer locking [4,5]. Due to spin conservation in optical dipole transitions, IXs form within the same spin-oriented bands of adjacent layers [4]. To confirm that the assigned peaks are IXs, we have calculated the exciton wave function which shows the charge density plot of the electron by keeping the hole position fixed very close to the transition metal position, as shown in Fig. 3(a). As can be noticed from the figure, the A exciton is confined within one layer, suggesting an intralayer-exciton-like nature. On the other hand, IX is delocalized in neighboring layers, indicating interlayer characteristics.

Likewise, we observe IX in the $Mo_{0.5}W_{0.5}Se_2$ single crystal [see Fig. 3(c)]; however, a relatively broad and weak feature of IX is detected. This can be attributed to the weak interlayer coupling between the bands due to the larger spin-orbit splitting of the electronic bands [3,57], i.e., $Mo_{0.5}W_{0.5}Se_2$ exhibits spin-orbit splitting larger than that of $Mo_{0.5}W_{0.5}S_2$ [see Figs. 3(b) and 3(c)]. This fosters stronger interlayer coupling, forming an IX of larger oscillator strength in $Mo_{0.5}W_{0.5}S_2$ compared to $Mo_{0.5}W_{0.5}Se_2$. In contrast to $Mo_{0.5}W_{0.5}Se_2$, this IX becomes less discernible at room temperature in $Mo_{0.5}W_{0.5}S_2$. This may be due to the delocalization of carriers caused by high carrier-phonon scattering in sulfides, as noticed from high longitudinal optical (LO) phonon energy in our phonon calculations discussed later. Further, we extended our analysis to include monolayers for the completeness of our theoretical calculation. As expected, in the case of monolayers, we did not observe any signature of the IX (see Fig. S13 [19]).

D. A′ and B′ excitons in bulk $Mo_{0.5}W_{0.5}S_2$ single crystal

Another noteworthy observation of our study is the demonstration of highly energetic A′ and B′ excitons originating

from the SOC split valance band at the K valley (V_1 and V_2 to the higher conduction band since the energy separation of these features are same as that of A and B excitons (see Fig. S11 [19]). While the experimental identifications of these A′ and B′ excitons have been previously reported in materials like $MoSe_2$ [18], WSe_2 [16,17], and $MoTe_2$ [15,18], it is important to note that their presence has not yet been experimentally demonstrated in any sulfide TMDs in monolayer or bulk, despite the theoretical predictions [7,58]. The theoretical analysis suggests that the large size of anion atoms is not only responsible for the observation of A′ and B′ excitons but also for influencing the electron-phonon interactions depending on the excitonic energies [7]. This means, at higher temperatures, electron-phonon interactions affect the higher-energy excitons more strongly than the lower-energy excitons. As a result, higher-energy excitonic peaks merge into a much broader peak and so could not be resolved in the experiments at relatively high temperatures. We conducted comprehensive temperature-dependent reflectance measurements from 4 to 300 K to address this, as presented in Figs. 3(b) and 3(c). This analysis revealed that, at the lowest temperature of 4 K, we could distinctly observe the sharp A′ and B′ excitons in bulk $Mo_{0.5}W_{0.5}S_2$ single crystal. However, as the temperature increased, they coalesced into much broader peaks and become less prominent at room temperature. Contrastingly, A′ and B′ excitons observed in bulk $Mo_{0.5}W_{0.5}Se_2$ single crystal are less affected by temperature [Fig. 3(c)]. To understand the mechanism and role played by phonons in the broadening of A′ and B′ excitons, we have calculated the phonon dispersion curves of both alloys in Fig. S14 [19]. More details are in the SM [19] and Refs. [59–61]. Due to the heavier atomic weight of Se atoms, $Mo_{0.5}W_{0.5}Se_2$ phonon bands are shifted downwards to the lower frequencies compared to their sulfides. This signifies that carrier-phonon interactions become more significant in $Mo_{0.5}W_{0.5}Se_2$ due to high LO phonon energy of $\sim$45 meV in

comparison to $Mo_{0.5}W_{0.5}Se_2$ ($\sim$32 meV). As a result, highly energetic A′ and B′ excitons in $Mo_{0.5}W_{0.5}S_2$ are becoming much broader and weaker at higher temperatures, but are clearly observed as sharper peaks at low temperatures. In contrast, weaker carrier-phonon interaction in $Mo_{0.5}W_{0.5}Se_2$ is not affecting these excitons at room temperature, similar to previous reports of transition metal selenides [15–18] and tellurides [15,18].

III. CONCLUSIONS

In conclusion, temperature-dependent reflectance spectroscopy, in conjunction with theoretical calculations, demonstrates various optically active transitions in bulk $Mo_{0.5}W_{0.5}S_2$ and $Mo_{0.5}W_{0.5}Se_2$ alloy single crystals. Apart from intralayer, interlayer, and highly energetic A′ and B′ excitons, we also observe Rydberg excitons in both systems. Temperature-dependent studies show that at higher temperatures electron-phonon interactions affect the higher-energy excitons more strongly than the lower-energy excitons. Our comprehensive study reveals these exotic excitonic states on a single platform, which will help to understand the fundamental physics and may open up opportunities for the implementation of Bose-Einstein condensation, quantum information processing and optoelectronic applications at room temperature.

[1] G. Wang, A. Chernikov, M. M. Glazov, T. F. Heinz, X. Marie, T. Amand, and B. Urbaszek, Rev. Mod. Phys. **90**, 021001 (2018).

[2] A. Chernikov, T. C. Berkelbach, H. M. Hill, A. Rigosi, Y. Li, B. Aslan, D. R. Reichman, M. S. Hybertsen, and T. F. Heinz, Phys. Rev. Lett. **113**, 076802 (2014).

[3] I. C. Gerber *et al.*, Phys. Rev. B **99**, 035443 (2019).

[4] J. Horng, T. Stroucken, L. Zhang, E. Y. Paik, H. Deng, and S. W. Koch, Phys. Rev. B **97**, 241404(R) (2018).

[5] A. Arora *et al.*, Nat. Commun. **8**, 639 (2017).

[6] C. Schneider, M. M. Glazov, T. Korn, S. Höfling, and B. Urbaszek, Nat. Commun. **9**, 2695 (2018).

[7] D. Y. Qiu, F. H. da Jornada, and S. G. Louie, Phys. Rev. Lett. **111**, 216805 (2013).

[8] D. Xiao, G.-B. Liu, W. Feng, X. Xu, and W. Yao, Phys. Rev. Lett. **108**, 196802 (2012).

[9] C. Mai, A. Barrette, Y. Yu, Y. G. Semenov, K. W. Kim, L. Cao, and K. Gundogdu, Nano Lett. **14**, 202 (2014).

[10] H. M. Hill, A. F. Rigosi, C. Roquelet, A. Chernikov, T. C. Berkelbach, D. R. Reichman, M. S. Hybertsen, L. E. Brus, and T. F. Heinz, Nano Lett. **15**, 2992 (2015).

[11] S. Y. Chen *et al.*, Nano Lett. **19**, 2464 (2019).

[12] J. Shi, Z. Lin, Z. Zhu, J. Zhou, G. Q. Xu, and Q. H. Xu, ACS Nano **16**, 15862 (2022).

[13] K. R. Hansen, J. S. Colton, and L. Whittaker-Brooks, Adv. Opt. Mater. **12**, 2301659 (2024).

[14] S. Zheng, L. Sun, X. Zhou, F. Liu, Z. Liu, Z. Shen, and H. J. Fan, Adv. Opt. Mater. **3**, 1600 (2015).

[15] A. R. Beal, J. C. Knights, and W. Y. Liang, J. Phys. C: Solid State Phys. **5**, 3540 (1972).

[16] W. Zhao, Z. Ghorannevis, L. Chu, M. Toh, C. Kloc, P. H. Tan, and G. Eda, ACS Nano **7**, 791 (2013).

[17] A. J. Grant, J. A. Wilson, and A. D. Yoffe, Philos. Mag. **25**, 625 (1972).

[18] J. A. Wilson and A. D. Yoffe, Adv. Phys. **18**, 193 (1969).

[19] See Supplemental Material at http://link.aps.org/supplemental/10.1103/PhysRevB.110.075205 for details of structural and compositional properties of bulk alloy single crystals, details of theoretical calculations and temperature-dependent reflectance spectroscopy, angle-resolved photoemission spectroscopy, Rydberg excitons in bulk alloy single crystals for other temperature,

calculated absorption spectrum for monolayer alloys, and phonon dispersion curves.

[20] A. F. Rigosi, H. M. Hill, K. T. Rim, G. W. Flynn, and T. F. Heinz, Phys. Rev. B **94**, 075440 (2016).

[21] G. Wang *et al.*, Nat. Commun. **6**, 10110 (2015).

[22] H. Shi, R. Yan, S. Bertolazzi, J. Brivio, B. Gao, A. Kis, D. Jena, H. G. Xing, and L. Huang, ACS Nano **7**, 1072 (2013).

[23] X. Wang, G. Niu, J. Jiang, L. Sui, X. Zeng, X. Liu, Y. Zhang, G. Wu, K. Yuan, and X. Yang, J. Phys. Chem. Lett. **13**, 10395 (2022).

[24] P. D. Cunningham, A. T. Hanbicki, K. M. McCreary, and B. T. Jonker, ACS Nano **11**, 12601 (2017).

[25] A. Arora, K. Nogajewski, M. Molas, M. Koperski, and M. Potemski, Nanoscale **7**, 20769 (2015).

[26] J. Kang, Y. Wang, L. Zhou, O. A. Al-Hartomy, S. Wageh, Y. Wang, H. Zhang, S. Xiao, and J. He, Appl. Phys. Lett. **123**, 061107 (2023).

[27] S. Biswas *et al.*, ACS Nano **17**, 7685 (2023).

[28] Z. Wang, D. A. Rhodes, K. Watanabe, T. Taniguchi, J. C. Hone, J. Shan, and K. F. Mak, Nature (London) **574**, 76 (2019).

[29] P. Taank, R. Karmakar, R. Sharma, R. K. Yadav, M. Shrivastava, N. C. Maurya, T. K. Maji, D. Karmakar, and K. V. Adarsh, J. Phys. Chem. C **126**, 416 (2022).

[30] D. Mandal, M. Shrivastava, S. Sharma, A. K. Poonia, S. Marik, R. P. Singh, and K. V. Adarsh, ACS Appl. Nano Mater. **5**, 5479 (2022).

[31] K. Bogaert, S. Liu, T. Liu, N. Guo, C. Zhang, S. Gradečak, and S. Garaj, Sci. Rep. **8**, 12889 (2018).

[32] Z. Hemmat *et al.*, Adv. Mater. **32**, 1907041 (2020).

[33] P. Taank, A. Raji, R. S. Singh, and K. V. Adarsh, Fine structure splitting and exciton interactions in $MoWSe_2$ single-crystal, *Conference on Lasers and Electro-Optics, San Jose, California* (Optica Publishing Group, 2022), p. SF4K.6.

[34] L. Wu *et al.*, ACS Nano **15**, 8397 (2021)

[35] P. E. Blöchl, Phys. Rev. B **50**, 17953 (1994).

[36] G. Kresse and J. Furthmüller, Phys. Rev. B **54**, 11169 (1996).

[37] J. P. Perdew, K. Burke, and M. Ernzerhof, Phys. Rev. Lett. **77**, 3865 (1996).

[38] L. Bellaiche and D. Vanderbilt, Phys. Rev. B **61**, 7877 (2000).

[39] L. Hedin, Phys. Rev. **139**, A796 (1965).

[40] M. Shishkin and G. Kresse, Phys. Rev. B **74**, 035101 (2006).

[41] A. A. Mostofi, J. R. Yates, Y. S. Lee, I. Souza, D. Vanderbilt, and N. Marzari, Comput. Phys. Commun. **178**, 685 (2008).

[42] V. Wang, N. Xu, J. C. Liu, G. Tang, and W.-T. Geng, Comput. Phys. Commun. **267**, 108033 (2021).

[43] T. Cheiwchanchamnangij and W. R. L. Lambrecht, Phys. Rev. B **85**, 205302 (2012).

[44] H. Terrones, F. Lòpez-Uròas, and M. Terrones, Sci. Rep. **3**, 1549 (2013).

[45] J. Xiao, M. Zhao, Y. Wang, and X. Zhang, Nanophotonics **6**, 1309 (2017).

[46] E. E. Salpeter and H. A. Bethe, Phys. Rev. **84**, 1232 (1951).

[47] P. Taank, R. Karmakar, and K. V. Adarsh, Surf. Interface Anal. **55**, 521 (2023).

[48] E. Liu, J. van Baren, T. Taniguchi, K. Watanabe, Y.-C. Chang, and C. H. Lui, Phys. Rev. B **99**, 205420 (2019).

[49] A. Raja *et al.*, Nano Lett. **18**, 6135 (2018).

[50] X. L. Yang, S. H. Guo, F. T. Chan, K. W. Wong, and W. Y. Ching, Phys. Rev. A **43**, 1186 (1991).

[51] T. Kazimierczuk, D. Fröhlich, S. Scheel, H. Stolz, and M. Bayer, Nature (London) **514**, 343 (2014).

[52] V. V. Zalamai, N. N. Syrbu, I. G. Stamov, and S. I. Beril, J. Opt. **22**, 085402 (2020).

[53] K. Reimann, M. Steube, D. Fröhlich, and S. J. Clarke, J. Cryst. Growth **189**, 652 (1998).

[54] S. Faure, T. Guillet, P. Lefebvre, T. Bretagnon, and B. Gil, Phys. Rev. B **78**, 235323 (2008).

[55] G. Zhang, A. Chaves, S. Huang, F. Wang, Q. Xing, T. Low, and H. Yan, Sci. Adv. **4**, eaap9977 (2018).

[56] J. Deslippe, M. Dipoppa, D. Prendergast, M. V. O. Moutinho, R. B. Capaz, and S. G. Louie, Nano Lett. **9**, 1330 (2009).

[57] A. R. Beal and W. Y. Liang, J. Phys. C: Solid State Phys. **9**, 2459 (1976).

[58] R. V. Kasowski, Phys. Rev. Lett. **30**, 1175 (1973).

[59] A. Togo, L. Chaput, T. Tadano, and I. Tanaka, J. Phys.: Condens. Matter **35**, 353001 (2023).

[60] Y. Ikeda, A. Carreras, A. Seko, A. Togo, and I. Tanaka, Phys. Rev. B **95**, 024305 (2017).

[61] K. Kaasbjerg, K. S. Thygesen, and K. W. Jacobsen, Phys. Rev. B **85**, 115317 (2012).